AGU PUBLICATIONS

JGR

Journal of Geophysical Research: Oceans

RESEARCH ARTICLE

10.1002/2015JC011287

Special Section:
Forum for Arctic Modeling and Observational Synthesis (FAMOS): Results and Synthesis of Coordinated Experiments

An inverse modeling study of circulation in the Eastern Bering Sea during 2007–2010

Gleb Panteleev[1,2], Max Yaremchuk[3], Oceana Francis[4], Phyllis J. Stabeno[5], T. Weingartner[6], and J. Zhang[7]

[1]International Arctic Research Center, University of Alaska, Fairbanks, Alaska, USA, [2]National Tomsk Research Polytechnic University, Tomsk, Russia, [3]Naval Research Laboratory, Stennis Space Center, Mississippi, USA, [4]Department of Civil and Environmental Engineering, University of Hawaii, Honolulu, Hawaii, USA, [5]Pacific Marine Environmental Laboratory, National Atmospheric and Oceanic Administration, Seattle, Washington, USA, [6]School of Fisheries and Marine Science, University of Alaska, Fairbanks, Alaska, USA, [7]Applied Physics Laboratory, University of Washington, Seattle, Washington, USA

Abstract A two-way nested 4d-variational data assimilation system is implemented in the Eastern Bering Sea (EBS) to investigate changes in circulation and thermodynamic state for a 3.8 year period. Assimilated observations include data from 19 moorings deployed on the shelf and in the Bering Strait, 1705 hydrographic stations occupied during eight surveys, and remotely sensed sea surface temperature and sea surface height (SSH) data. Validation of the presented 4dVar reanalysis against the output of two sequential data-assimilative systems (the Bering Ecosystem Study ice-ocean Modeling and Assimilation System (BESTMAS) and the Arctic Cap Nowcast-Forecast System (ACNFS)) has shown that the product is more consistent with the observed transports in the Bering Strait and in the EBS interior both in terms of their magnitude and time variability. Analysis of the data-optimized solution quantifies a sequence of wind-forced events that resulted in the anomalous heat and freshwater transports through the Bering Strait, including a 28 day long flow reversal that occurred in November 2009 and carried Siberian Coastal Current water down to the Gulf of Anadyr. Lagrangian study of the Arctic-bound Pacific waters indicates the extreme importance of the cross-shelf exchange along the path of the Bering Slope Current and quantifies the spectrum of residence times for the waters entering EBS through Unimak Pass and through Aleutian passages. Residence times in the EBS cold pool are diagnosed to be 2–3 times longer than those in the surrounding waters.

Key Points:
- Circulation in the Eastern Bering Sea can be reconstructed through the nested data assimilation
- Two way nested data assimilation approach converges
- Transport estimates and particle study are conducted

Correspondence to:
G. Panteleev,
gleb@iarc.uaf.edu

Citation:
Panteleev, G., M. Yaremchuk, O. Francis, P. J. Stabeno, T. Weingartner, and J. Zhang (2016), An inverse modeling study of circulation in the Eastern Bering Sea during 2007–2010, *J. Geophys. Res. Oceans*, *121*, 3970–3989, doi:10.1002/2015JC011287.

Received 1 SEP 2015
Accepted 18 FEB 2016
Accepted article online 26 FEB 2016
Published online 12 JUN 2016

© 2016. American Geophysical Union. All Rights Reserved.

1. Introduction

With the ongoing increase of the Arctic temperature, oceanography in the Bering Sea (BS) has been the subject of intensifying research in recent years [e.g., *Hu and Wang*, 2010; *Ezer and Oey*, 2010; *Grebmeier and Maslowski*, 2014, and references therein]. Importance of the Eastern Bering Sea (EBS) basin (Figure 1) cannot be overlooked, as it controls the only pathway between the Pacific and Arctic oceans and appears one of the most productive ecosystems in the world. At the same time, decreasing EBS ice cover and complexity of the cross-shelf processes pose challenging tasks in estimating and predicting changes in the import of Pacific water into the Arctic and evolution of the local ecosystem.

A number of efforts to meet these challenges was made recently by the numerical modeling community. Numerous studies were executed at resolutions of up to several kilometers, focusing on the BS state variability from inter-annual to seasonal scales. As a few examples, *Clement et al*. [2005] simulated the long-term (1979–2001) variations in the BS circulation under ECMWF forcing at 9 km resolution and obtained, in particular, a strong evidence of wind control over the Bering Strait transport (BST), whose 23 year mean values was estimated to be 0.67 Sv. The mean seasonal cycle of the BS circulation in the period between 1996 and 2006 was studied at 8 km resolution by *Wang et al*. [2009], who obtained a somewhat larger BST of 0.8 ± 0.33 Sv and identified two opposed surface circulation regimes controlled by the seasonal changes in wind forcing. In a later 7 km resolution study, *Wang et al*. [2013] focused on simulation of the plankton and sea ice variations during the field campaigns of 2007 and 2008 and found that the largest impact on bioproductivity on the BS shelf is given by changes in air temperature.

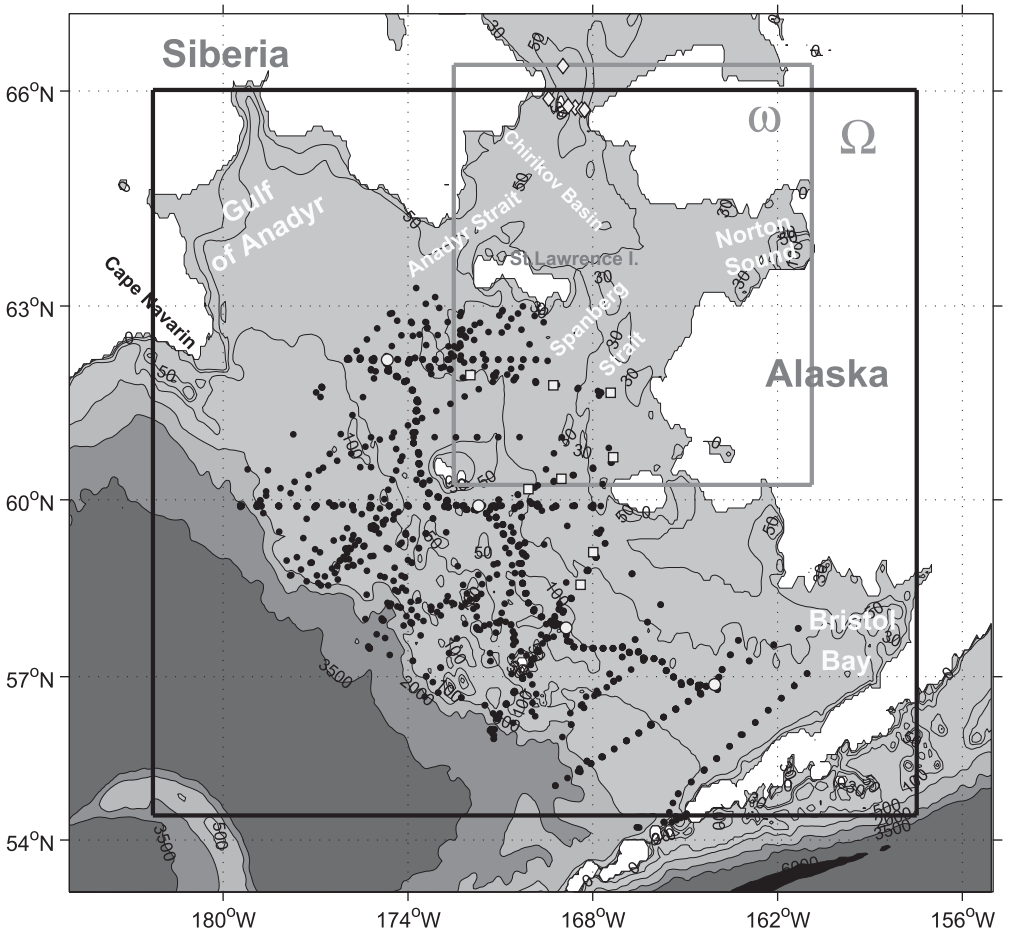

Figure 1. Model domain and assimilated observations. The boundaries of the coarse (17 km) and fine (7 km) resolution grids are shown by the black and gray rectangles. Black circles show hydrographic stations, mooring locations from different observational experiments are shown as white circles, squares and diamonds.

An interesting conceptual model of the BST was proposed recently by *Danielson et al*. [2014], who argued, in particular, that increasing of storm activity over the BS tends to decrease the northward BST at annual to decadal time scales, and, therefore, inhibit desalinization of the Arctic basin by the Pacific water inflow. Extreme importance of the winds in controlling the EBS circulation was also pointed out in earlier studies by *Danielson et al*. [2011, 2012a]. Most recently, *Durski et al*. [2015] investigated summer (June–October 2009) circulation in EBS at 2 km resolution and underlined a significant role of tidal forcing on the EBS shelf dynamics.

The outlined studies were targeted at the analyses of various phenomena and/or circulation modeling on much larger scales (e.g., Arctic Ocean). For example, *Danielson et al*. [2014] utilized the barotropic version of the ROMS ocean model to study the wind impact on the dynamics of the Bering Sea shelf and shelf break. *Durski et al*. [2015] analyzed the impact of tides on the erosion of the cold water mass in the central EBS during the summer. This body of water with bottom temperatures below 2°C (known as "cold pool" in the literature [e.g., *Cianelli and Bailey*, 2005]) is maintained by winter cooling and plays an important role for the Bering Sea ecosystem. In the summer the cold pool imposes a natural barrier separating cod population in the outer Bering Sea shelf and capelin population that prefers EBS coastal areas Thus, the processes responsible for erosion of the cold pool are important for understanding migration pathways of the forage fish population in the Bering Sea [*Cianelli and Bailey*, 2005; *Stabeno et al*., 2012; *Zador et al*., 2012].

A recent overview of the most advanced BS models by *Clement-Kinney et al*. [2014] have also shown that there is still a large scatter in the Bering Strait transport estimates, although a certain trend to smaller (0.7–0.8 Sv) BST values with increasing grid resolution has been documented. The authors conclude, that

despite relatively high (0.6–0.8) correlations between the simulated and observed transports, there is still a need for higher spatial resolution and additional measurements with better spatial coverage to reduce the uncertainties and constrain the model solutions. Insufficient accuracy of the BST simulation indicates that despite a reasonably good consistency between the models and available data, significant improvement of the forecast skill and the related process studies can only be achieved by the synthesis of model dynamics with observations. The EBS reanalysis conducted in this way allows us to obtain a more accurate reconstruction of the sea state which is statistically consistent with all the available data, while being simultaneously constrained by the model dynamics. In particular, a dynamically consistent and accurate fit to the data is very important for the proper description of the regional ecosystem where accurate simulation of the advection processes and hydrophysical conditions (temperature and salinity) are a critical issue [*Panteleev et al*., 2004].

Unfortunately, data assimilation studies of the region are much less numerous. The Arctic Cap Nowcast-Forecast System (ACNFS) run by the Naval Research Laboratory since 2007 [*Posey et al*., 2010; *Allard et al*., 2012] assimilates remotely sensed data providing daily analyses and forecasts of the ocean and ice fields north of 50°N at 10 km resolution. However, the ACNFS output was overlooked by the academic community partly because of somewhat limited access.

The first regional data assimilation model for the Northern Bering and Chukchi seas was proposed by *Brasseur* [1991]. The model was constrained by steady-state quasigeostrophic dynamics and was successful in explaining what were the driving mechanisms of the primary productivity in the Northern Bering Sea [*Brasseur and Hausk*, 1991; *Nihoul et al*., 1993]. Among more recent regional data assimilation studies available in literature, *Panteleev et al*. [2006] assessed the mean summer Kamchatka Current transport using 4d-variational (4dVar) assimilation of climatological data into a primitive equation model. Later, *Panteleev et al*. [2010] investigated 1990–1991 circulation north of the Bering Strait to identify the pathways and residence times of the Pacific Water in the Chukchi Sea. Similar approach was also successfully utilized for the reconstruction of the mean dynamic ocean topography in the Bering Sea [*Panteleev et al*., 2011a]. Most recently, a number of in-depth studies of the EBS circulation has been made using the Bering Ecosystem Study ice-ocean Modeling and Assimilation System (BESTMAS) which assimilates sea ice data and sea surface temperature from satellites using a sequential technique based on the optimal interpolation algorithm [*Lindsay and Zhang*, 2006]. The system was developed at the Applied Physics Laboratory, University of Washington [*Zhang and Rothrock*, 2001, 2005; *Zhang et al*., 2010] and runs at 7 km horizontal resolution.

Detailed studies and continuous monitoring of the EBS shelf lead to a demand for further expansion of in situ observations. Of particular interest are velocity observations at the EBS shelf, where a number of moorings have been deployed since 1995 [*Stabeno et al*., 2010] and supplemented by several hydrographic surveys. In addition, the Bering Strait has been monitored for 26 years by a limited mooring array of 1–4 moorings [*Roach et al*., 1995; *Woodgate et al*., 2005] that was recently expanded to provide a clearer view of the cross-strait flow [*Woodgate et al*., 2012, 2015]. In 2008–2009, extensive observations were conducted at the central EBS shelf in the framework of the BS Ecosystem Study (BEST) and the BS Integrated Ecosystem Research Program (BSIERP). The core of these experiments were seasonal hydrographic surveys and nine moorings in the outer parts of the EBS shelf [*Danielson et al*., 2012b]. In the present study, all the above mentioned data are combined with the BS climatology [*Panteleev et al*., 2011b, 2013], and synthesized with model dynamics using a two-way nested 4dVar data assimilation technique.

The major objective of the paper is to perform a dynamically and statistically consistent reanalysis of the 2007–2010 EBS circulation, and quantify some of the issues important to bioproductivity of the EBS shelf, such as pathways and residence times of the Pacific waters, their rates of exchange at the shelf break and through the Bering Strait. In addition, we provide new estimates of the BST and associated heat and freshwater fluxes, compare the results with the output of ACNFS and BESTMAS data assimilative systems, assess the impact of the wind-blocking event on the BST observed in October–November 2009, and identify the reasons of the anomalous heat and freshwater transports through the Bering Strait observed in July–November of 2007 and 2010.

The paper is organized as follows. In the next section, we describe the numerical model, the two-way nested 4dVar technique, and the data used in assimilation. Section 3 contains validation of the optimized solution against observations and ACNFS/BESTMAS output, Lagrangian analysis of the reconstructed

circulation, and assessment of the BST variability with a special focus on wind-blocking events. Summary and discussion in section 4 complete the paper.

2. Methodology

2.1. Dynamically Constrained 4-D Interpolation

The dynamical constraints used for space-time interpolation of the data are provided by the Semi-implicit ocean model (SIOM), that have been successfully used in a number of data-assimilation studies of the Bering [*Panteleev et al*., 2006, 2011a, 2012] and Chukchi [*Panteleev et al*., 2010] seas.

One of the major objectives of the present study is to quantify the dynamics of communication between the Arctic and Pacific oceans through the Bering Strait. Because circulation in the EBS shelf is characterized by barotropic dynamics most of the year, velocity and SSH data are the key observational quantities controlling the total transport field. Therefore, in designing the inverse model, special attention was paid to accurate assimilation of all available SSH and velocity observations. This requirement imposed a rather high limit (5–7 km) on the model resolution due to 10–15 km spacing between the velocity observation points in the 85 km wide Bering Strait. On the other hand, available SSH data (section 2.3.4) have a typical horizontal resolution of 30–40 km and are unavailable in northern EBS for almost half a year because of the ice cover. Guided by these considerations, we designed two-way nested 4dVar system with a fine (7 km) model grid ω embedded into a coarser (15–20 km) grid Ω (Figure 1). In the vertical, the coarse(fine) resolution model had 35(15) unevenly spaced levels with 5(2.5) m near-surface spacing which increased to 500(25) m at the bottom.

Trajectories $\mathbf{x}(t)$ of both models were controlled by the initial/boundary conditions and surface fluxes. The grid point values of the corresponding fields $\mathbf{x}(0), \mathbf{x}_b(t_n) \in \mathbf{x}(t_n)$, and $\mathbf{x}_f(t_n)$ were adjusted to minimize discrepancy with observations which was measured by the following cost function:

$$J^0 = \frac{1}{2}(\mathbf{Hx}-\mathbf{d})^{\mathbf{T}}\mathbf{R}^{-1}(\mathbf{Hx}-\mathbf{d}) + \frac{1}{2}(\mathbf{x}-\mathbf{x}^b)^{\mathbf{T}}\mathbf{B}^{-1}(\mathbf{x}-\mathbf{x}^b) + \\ + \frac{1}{2}(\mathbf{x}_f-\mathbf{x}_f^b)^{\mathbf{T}}\mathbf{B}_f^{-1}(\mathbf{x}_f-\mathbf{x}_f^b), \tag{1}$$

where $\mathbf{x}$ is the set of grid point values of the model fields, $\mathbf{Hx}$ is the result of SIOM integration sampled at the observational space-time locations, $\mathbf{R}$ is the representational error covariance of the observations, $\mathbf{x}^b$ is the background EBS climatology, $\mathbf{x}_f^b$ stands for the background surface fluxes, and $\mathbf{B}$, $\mathbf{B}_f$ are the respective error covariance matrices. The matrix $\mathbf{R}$ was diagonal with error variances described in section 2.3. A detailed description of observations $\mathbf{d}$, background surface fluxes $\mathbf{x}_f^b$, the EBS climatology $\mathbf{x}^b$ and their error variances are given in sections 2.3.1–4, 2.3.5 and 2.3.6, respectively. The inverse covariances $\mathbf{B}^{-1}$ and $\mathbf{B}_f^{-1}$ were modeled by the quadratic polynomials of the Laplacian operator [*Yaremchuk and Sentchev*, 2012] with the decorrelation scale specified by the model grid step.

At the first iteration, the minimization was performed in a conventional one-way nesting manner on a sequence of 1 month time intervals (assimilation windows) within the time interval $T = 1372$ days spanning the period from 1 January 2007 to 3 October 2010. The optimal model state $\mathbf{x}$ at the end of a window was taken as the first guess for the initial conditions $\mathbf{x}(0)$ of the next window. At the open boundaries, the background values of control variables (part of the second term in equation (1)) were taken from the BESTMAS solution in Ω from the northern boundary of ω and from the optimized coarse grid solution at the southern and western boundaries of ω, i.e., assimilation in ω was performed after the completion of assimilation in Ω, using the coarse grid solution for the open boundary control, where available. In time, the open boundary conditions for both models were parameterized using piecewise linear functions with 7 day discretization.

The method described above is similar to the one-way 4dVar nested algorithm of *Jankovic et al*. [2013]. In the considered application, however, such approach may provide inaccurate results for two reasons. First, the general features of circulation in Ω are largely defined by the choke point (Bering Strait) transport, which can be accurately optimized on the fine grid ω. At the same time, relatively coarse SSH data, capable of constraining large-scale circulation features in Ω and providing suboptimal boundary conditions for ω, are more abundant in the southern parts of the coarse resolution domain. Another reason for the two-way nested design was due to prohibitive computational expense of configuring the inverse model in Ω at fine resolution. Effective filtering of spurious gravity waves by semi-implicit numerics comes at the expense of

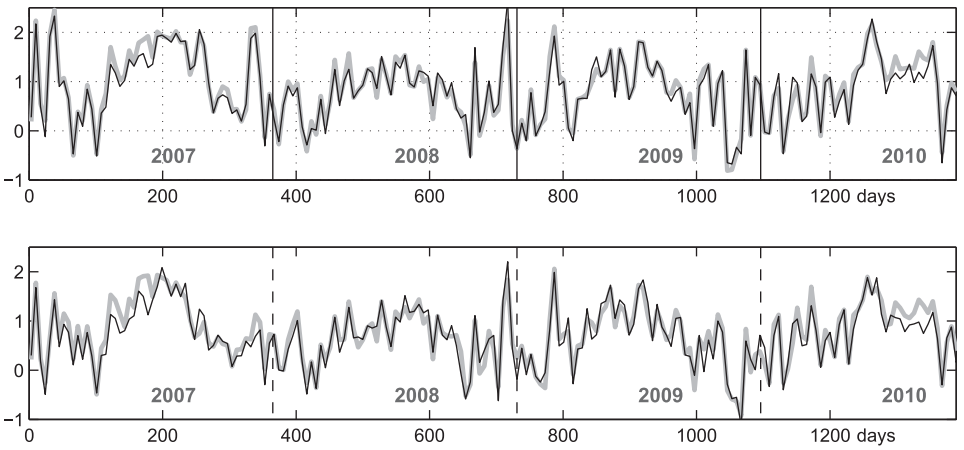

Figure 2. Transport (Sv) through the (top) Bering Strait and (bottom) western open boundary of the fine resolution domain ω after four iterations of the two-way 4dVar optimization. Transport values for the fine and coarse resolution domains are shown respectively by thick gray and thin black lines.

computation time which grows quadratically with the number of grid points. These considerations lead to the nested 4dVar design with the two-way communication between the impacts of fine and coarse resolution data sets which constrain model solutions on the respective grids.

2.2. Two-way 4dVar Nesting Technique

Coupling between the 4dVar problems was introduced by the following iterative process. After finding suboptimal solutions $\mathbf{x}_\Omega^n(t)$ and $\mathbf{x}_\omega^n(t)$ on the nth iteration, cost functions on the next iteration were updated as follows:

$$J_\Omega^{n+1} = J_\Omega^0 + \frac{\gamma}{2}[B(\mathbf{x}) - B(\mathbf{x}_\omega^n)]^2 \tag{2}$$

$$J_\omega^{n+1} = J_\omega^0 + \frac{3}{2}(\mathbf{x} - \mathbf{P}\mathbf{x}_\Omega^n)^{\mathbf{T}}\mathbf{B}^{-1}(\mathbf{x} - \mathbf{P}\mathbf{x}_\Omega^n), \tag{3}$$

where $B(\mathbf{x})$ is the BST corresponding to the model trajectory $\mathbf{x}(t)$ in the respective domain, $\mathbf{P}$ is the linear operator projecting coarse model fields within ω on the fine resolution grid [*Guidard and Fischer*, 2008], γ is a tunable relaxation weight, and the inverse background error covariance in (1) was multiplied by a factor of 3 to enforce the impact of observations in Ω on the dynamics in the fine resolution domain. It can be shown that in the linear case the iterative procedure (2–3) relaxes optimal solutions toward each other if the Hessian matrices of the uncoupled optimization problems have the full rank (see Appendix A). The optimal value of γ was assessed in a series of short-term assimilation experiments with the data available in September 2009. Distance D between the optimal solutions in Ω and ω was estimated in terms of the total transports through the Bering Strait and the open western boundary A of ω:

$$D(\mathbf{x}_\Omega, \mathbf{x}_\omega) = [B(\mathbf{x}_\Omega) - B(\mathbf{x}_\omega)]^2 + [A(\mathbf{x}_\Omega) - A(\mathbf{x}_\omega)]^2, \tag{4}$$

where squared differences between the transports were summed over the four weekly mean values. The optimal weight $\gamma = 250$ Sv^{-2} allowed reduction of the value of D by three times in four iterations for the experimental (monthly) run. When applied to the entire period of the integration, the reduction of D was even larger (4.3 times), while the correlation coefficients between the transports increased from 0.62 to 0.99 and from 0.53 to 0.98 respectively for the BST and the western boundary transport (Figure 2).

Similar convergence was obtained for the dominant patterns of spatial variability of the nested 4dVar solutions. Figures 3a–3d show the first two EOFs of the SSH variability in ω extracted from the fine and coarse grid 4dVar solutions at every 7 days on the fourth iteration. These two EOFs account for 85% and 90% of SSH variability of the optimal solutions on the coarse and fine resolution grids, respectively. Compared to uncoupled optimization, correlation between the EOF patterns increased from 0.71 to 0.98 for the first, and 0.64 to 0.97 for the second mode, whereas time correlations between their variability reached the values of 0.96 and 0.80 for the first EOF and second EOF respectively.

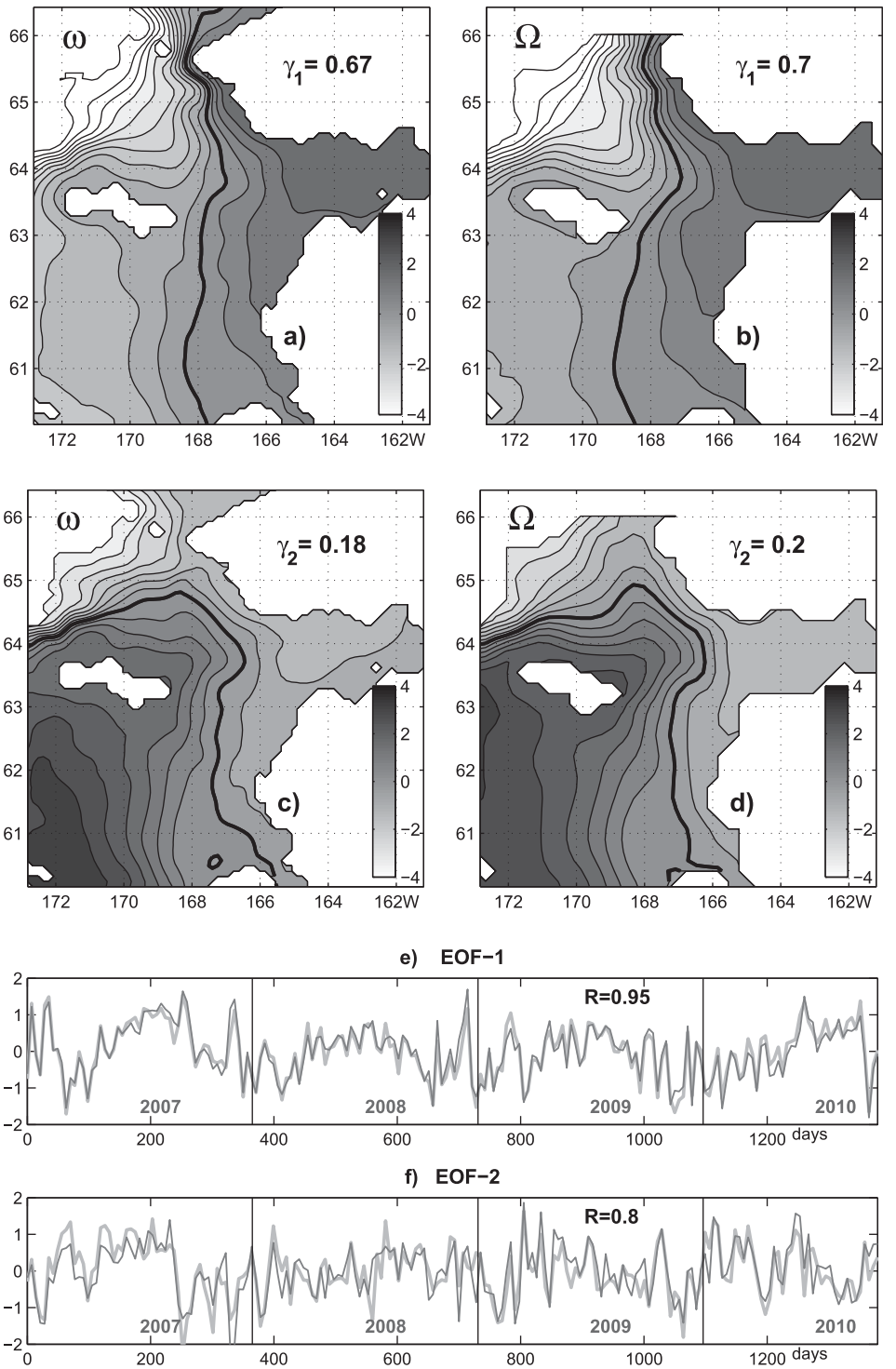

Figure 3. The first two EOFs of the SSH variability in ω for the (a, c) fine and (b, d) coarse resolution models after the completion of four nested 4dVar iterations. Coefficients $\gamma_{1,2}$ show the percentage of the SSH variance captured by the respective mode. Zero EOF contours are shown by thick lines. (e, f) show time variation of the first and second EOF's for the coarse (thick gray line) and high (thin black line) resolution models.

The described two-way nested 4dvar scheme allowed us to achieve much better consistency between the optimal solutions within the nested domains. As a result, a significantly better fit was also obtained to coarse resolution SSH data, constraining circulation in Ω, and higher resolution velocity data controlling the Bering Strait throughflow.

Variability of the first and second SSH EOFs in ω are shown at Figures 3e and 3f. The respective time series are correlated with the BST (Figure 2) at the levels of 0.97 and 0.15 respectively, suggesting that BST variability is mostly explained by the first EOF. The seasonal signal is clearly seen both in Figure 3e and the flow through the Being Strait (Figure 2). It was also found that both EOFs correlate significantly (at 0.73 and -0.52 respectively) with the transport through the Spanberg Strait, suggesting that the respective modes of SSH variation are responsible for the flow through the Spanberg Strait. In particular, the linear combination 2.57 EOF1 – 1.82 EOF2, has a 0.91 correlation with the flow through the Spanberg Strait, and may thus serve as a statistical tool for the diagnosis of the Spanberg Strait transport from satellite observations.

2.3. Data

The inverse modeling results presented in the next section are based on the comprehensive data set, which includes most of in situ and remotely sensed observations available for the region in 2007–2010. The total number of the observed temperature, salinity, velocity and SSH values constraining the model was 1,578,305.

2.3.1. Velocity

Velocity observations were taken from three mooring arrays permanently maintained in the Bering Strait, and on the EBS shelf (Figure 1). The Bering Strait array (shown by diamonds in Figure 1) provided velocity data at 10–55 km horizontal resolution during the entire period of our study. The total number of the supported moorings significantly varied during the period. On the average, there were 1–5 operating moorings east of the Diomede Islands (in the US side of the Bering Strait), 0–4 moorings west of the Diomedes, and one mooring approximately 55 km north of the islands. The total length of the velocity and temperature time series from these moorings spanned approximately 8500 days, i.e., on the average at a given time $8500/T = 6.2$ moorings were in operation from this group. A more detailed description of the Bering Strait mooring array is provided by *Woodgate et al*. [2015].

The second group of moorings (shown by circles in Figure 1) is maintained as a part of the EBS monitoring program funded by NOAA [*Stabeno et al*., 2001]. It includes four moorings deployed along the 80m isobath with spatial separation of approximately 500km. Moorings at 60° and 57° provided uninterrupted records during the entire assimilation period, while observations at two other moorings were available only in 2008–2010. The mean number of operating moorings in this group was 2.7.

The third set of the velocity observations includes nine moorings deployed along three lines in the central part of the EBS shelf (squares in Figure 1). This set of moorings included both ADCP and RCM instruments and was supported from July 2008 to July 2010 with the mean number of operating moorings 7.9 [*Danielson et al*., 2012b].

Approximately 80% of all the moorings were supplied by bottom mounted ADCP sensors. The remaining moorings had 1–2 velocity sensors below the surface ($\sim$ 20 m) and above the bottom. Velocity observations were preprocessed as follows. First, the velocity time series were low-pass filtered with a cutoff period of one week. Then the filtered velocities were interpolated in the vertical on the model grid. Due to higher errors of ADCP observations at the surface and near the bottom, the data within 5 m from the bottom and from surface were discarded.

To better constrain the barotropic mode, the preprocessed velocities derived from ADCP moorings were vertically averaged using cubic splines with zero derivatives at the end points, and these vertically averaged time series were also used in assimilation. The typical errors of the velocity observations were about 2–4 cm/s depending on the magnitude of the observed velocity vector. The total number of assimilated observations of the zonal and meridional velocity components was 17,876.

2.3.2. Temperature and Salinity

The core set of in situ temperature and salinity data comprised observations from multiple CTD surveys performed at the EBS in May–September (black dots in Figure 1) in the framework of the Bering sea Ecosystem STudy (BEST) and the Bering Sea Integrated Ecosystem Research Program (BSIERP) (http://beringsea.eol.ucar.edu/). These data were supplemented by the low pass filtered time series from temperature-conductivity sensors at the moorings.

Typically, two to three surveys were performed annually. Some of the surveys included transects along the 80 m isobath, performed at very high (10–15 km, Figure 1) resolution. In these cases the TS data were averaged over the respective model bins and the resulting mean profile was attributed to the center of the

corresponding grid cell. This averaging process allows us to assess the representation error, which was estimated by selecting pairs of stations separated by less than 20 km in space and 12 h in time and computing the mean absolute difference between the respective temperature and salinity readings. These computations produced an observation error root mean square (rms) variances of 0.1–0.75° C and 0.05–0.45 psu, depending on depth. It is also noteworthy that assessment of representation errors from the time filtering of the mooring records provided similar values. The total number of assimilated in situ temperature and salnity observations was 41,117.

2.3.3. Sea Surface Temperature

Satellite SST observations were taken from Operational Sea Surface Temperature and Sea Ice Analysis (OSTIA) product [*Stark et al*., 2007; *Donlon et al*., 2011] which provides daily maps at 1/20° resolution. The maps were interpolated on the model grids using bicubic splines and smoothed by the 2d Gaussian filter with the half-widths corresponding to the grid steps of the respective grids. SST errors were taken from the OSTIA data base and varied in space/time between 0.4 and 2.6°C with mean error of about 1° C. This level of accuracy is in agreement with the results of *Stroh et al*. [2016] who validated several SST products in the Arctic Ocean. The total number of assimilated SST observations was 888,822.

2.3.4. Sea Surface Height

The gridded SSH anomalies produced by Ssalto/Duacs (http://www.aviso.altimetry.fr/duacs/) and distributed by Aviso (http://www.aviso.altimetry.fr/en/data/products/sea-surface-height-products.html) were referenced to the regional mean dynamic ocean topography (MDOT) of *Panteleev et al*. [2011a] and assimilated. The AVISO maps of the SSH anomalies have a temporal resolution of 10 days and were linearly interpolated onto the model time grid. In the horizontal, the sum of MDOT and AVISO anomalies was projected on the model grid using bicubic splines.

SSH observation errors were assumed to have two statistically independent components: MDOT error estimated by *Panteleev et al*. [2011a], and the AVISO anomaly error, taken from the AVISO database at http://www.aviso.altimetry.fr/en/data/products/sea-surface-height-products.html. The resulting error fields varied in magnitude from 2 to 3 cm in the deep part of the EBS to 12–15 cm on the shelf, with the maximum values of 18–22 cm in the Gulf of Anadyr, Bristol Bay and Norton Sound. To avoid possible overfitting to less accurate SSH anomaly estimates in shallow (less than 40m) water, all SSH observations in these regions were excluded from assimilation, reducing the total number of SSH data points to 6,30,490.

2.3.5. Atmospheric Forcing

Near surface wind fields, heat and salt fluxes with spatial resolution of 6 h were taken from National Center for Environmental Prediction (NCEP) reanalysis (http://www.esrl.noaa.gov/psd/data/gridded/data.ncep.reanalysis.html). *Ladd and Bond* [2002] analyzed the quality of the NCEP surface fluxes over the Bering Sea and found significant errors in the summer heat fluxes over the EBS basin and wind speeds near the coastlines. We also found these data to be somewhat oversmoothed. To allow for the adjustment of the spatial details in the model forcing, we used surface flux data with relatively high error variances (up to 40% of their spatial and temporal variability in the EBS). The correlation scale was defined from statistical analysis of the 2006–2010 BETSMAS fluxes under the ice cover and from the respective NCEP fluxes in the ice-free regions.

The SIOM integration time (January 2007 to September 2010) involved several winter seasons, characterized by the ice cover over a significant part of the EBS. The background (NCEP) surface fluxes of momentum, heat and salt were replaced in the ice-covered regions by the respective ice-water fluxes from the BESTMAS solution, which assimilates sea ice parameters from the Special Sensor Microwave/Imager (SSMI) ice concentration delivered by the Hadley Center (http://hadobs.metoffice.com/hadisst [*Rayner et al*., 2003]). As it was shown in *Panteleev et al*. [2010], assimilating BESTMAS ice-ocean fluxes allows more accurate reconstruction of circulation in ice-covered regions than the use of NCEP forcing. This is due to relatively coarse resolution of the NCEP fluxes and a realistic screening effect of the ice cover reproduced by the BESTMAS solution.

The total number of surface flux data points used in assimilation was 3,501,904.

2.3.6. Climatological Background

Background information on the EBS hydrography was derived from the Climatological Atlas of the Bering Sea compiled by *Panteleev et al*. [2011b] from several data bases containing observations by American, Japanese, and Russian expeditions which took place between 1920 and 2008. These data were used to construct climatological means of temperature and salinity and standard deviations of these climatological mean values, which has been used in data assimilation. Temperature and salinity errors varied within 0.5° C

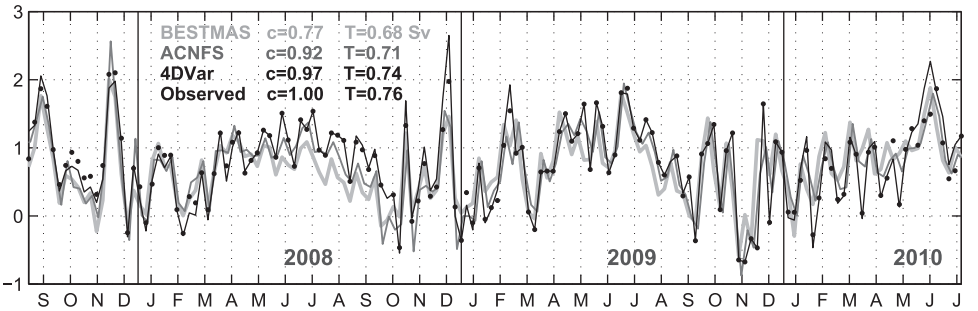

Figure 4. Weekly averaged Bering Strait transports (Sv) in the optimized solution (solid black line), and from the ACNFS (gray) and BESTMAS (light gray) output. Observed values are shown by solid dots. The time averaged values of the transport *T* and correlation coefficients *c* with observations are given.

– 1.5° C and 0.1 – 2.0 psu near the surface and decreased down to 0.1° C and 0.03 ppt, respectively in the deeper layers (below 1000 m). Seasonal temperature/salinity fields from the Atlas, as well as their errors were linearly interpolated in time and projected on the model grid using bicubic splines. The total number of temperature and salinity observations regridded from the Atlas was 14,131,305.

3. Results

3.1. Validation

The optimized evolution of EBS state was obtained by assimilating the above described data over 49 28 day time windows spanning the period from 1 January 2007 to 3 October 2010. On the average, 300 × 4 = 1200 iterations were required to achieve the nested 4dVar convergence of a single 4 week problem.

To estimate the quality of the data-optimized EBS evolution, it was compared with the output of the ACNFS and BESTMAS modeling systems which have similar spatial resolution but equipped with sequential data assimilation algorithms. Comparison was made in terms of the observed BST variability and the qualitative features of the regional circulation.

The weekly averaged velocity data from the Bering Strait moorings were optimally interpolated on the model grid with the horizontal and vertical decorrelation scales of 14 km and 10 m and then integrated over the Strait cross section to obtain the observed BST variability. For comparison purposes, these data were taken from the period between October 2007 and July 2010, when velocity observations were available at the Russian side of the Strait as well, so that the total number of operating moorings in the Bering Strait array was always larger than four.

Figure 4 compares Bering Strait transports of the three high-resolution data-assimilative models with observations. The 4dVar output shows better correspondence with observations both in terms of time variability (correlation) and the mean values. This is partly due to the fact that SIOM assimilates velocity data, whereas the other two models do not. On the other hand, the 4dVar solution is more strongly constrained dynamically as it is not forced by the nudging terms which attract model states to the data in ACNFS and BESTMAS solutions by introducing artificial forcing proportional to the model-data misfits.

Comparison of the 3.8 year mean BESTMAS and 4dVar SSH patterns (Figure 5) appears to favor the 4dVar solution. The patterns differ by the general structure of geostrophic currents in the Spanberg Strait separating Alaska from the St. Lawrence Island and across 60°N: The 4dVar solution is characterized by a weak northward flow at the surface, consistent with the general circulation pattern in EBS [*Stabeno et al.*, 1999, 2001; *Clement et al.*, 2005], while BESTMAS demonstrates nearly opposite flow along the Alaskan coast south of 63°N and the net southward transport across the southern boundary (Figure 5b). Since 4dVar corrections to wind forcing were relatively small, we attribute this difference to assimilation of the velocity observations in the Bering Strait and in the central EBS as well as SSH anomalies in the regions deeper than 40m. The 4dVar method dynamically propagates information from data-rich regions to the regions poorly covered by observations such as the Spanberg Strait through the adjustment of open boundary conditions. In particular, regional adjoint sensitivity analysis [*Panteleev et al.*, 2009] reveals moderate sensitivity of the Bering

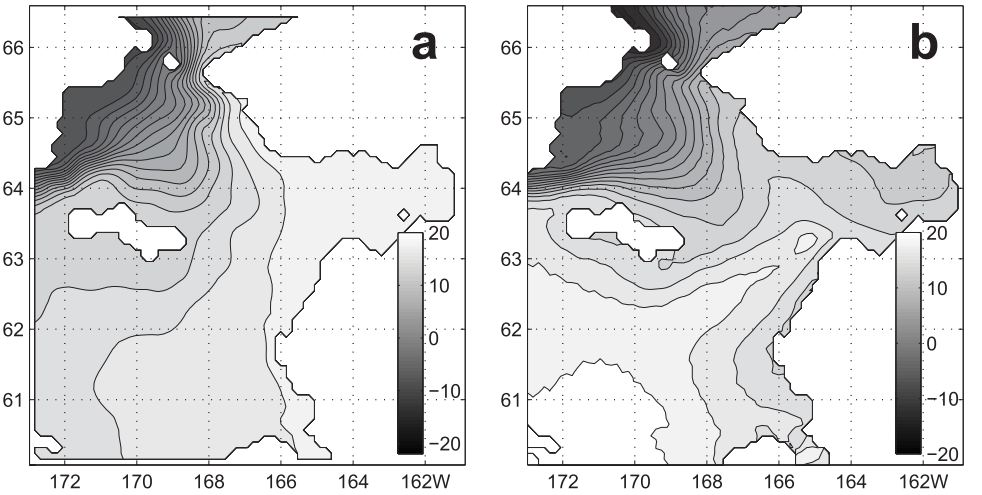

Figure 5. 3.8 year mean SSH (cm) for the (a) 4dVar and (b) BESTMAS solutions.

Strait transport estimates to observations along the eastern part of the St.Lawerence Island, suggesting long-range correlations induced by dynamics in the 4Dvar.

Figure 6 presents an illustration of improvement in the velocity model-data misfits compared to the BESTMAS solution. It is evident that 4dVar provides a considerable reduction of the velocity errors, especially in the EBS regions outside the Bering Strait (Figures 6a–6d) where rms discrepancies were reduced to 2–3 cm/s. The improvement is evident from comparison of the linear regression coefficients, *R*, between observed and modeled velocities which were typically several times closer to 1 than those derived from the BESTMAS solution.

Error reduction for the velocities observed in the Bering Strait (Figures 6e and 6f) is better visible in the range of weaker meridional velocities (0–0.4 m/s). For the entire range, 4dVar velocities demonstrate a

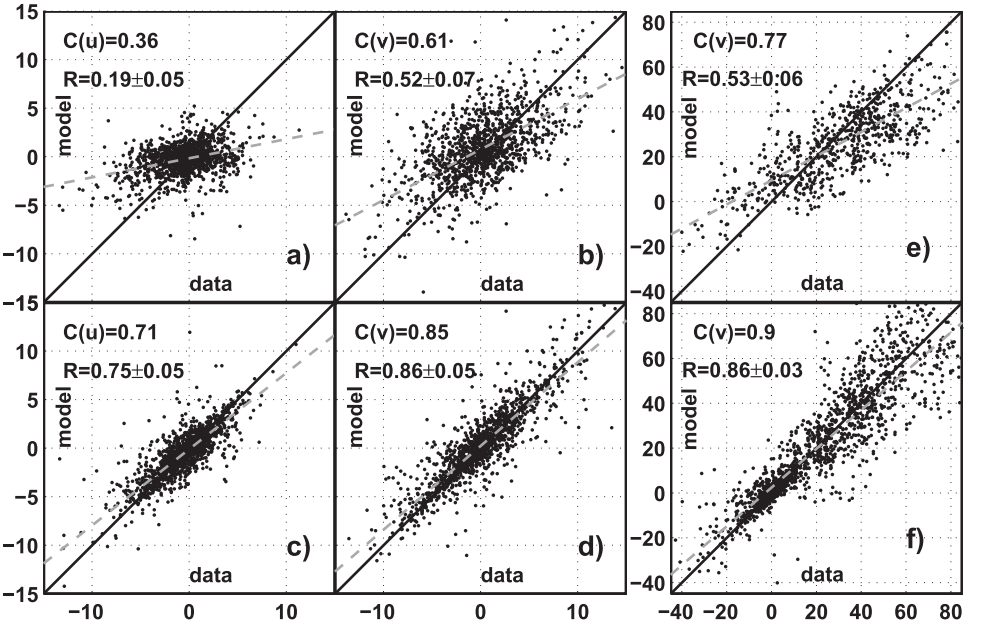

Figure 6. Scatter plots of the (a, c) zonal *u* and (b, d) meridional *v* velocity components against mooring observations (horizontal axes) for the (a, b) BESTMAS and (c, d) 4dVar solutions. (e, f) Similar relationship between the meridional velocity in the Bering Strait. Correlation coefficients and regression coefficient with 95% confidence intervals are shown in the top left corners of the figures. Dashed lines show the best linear fit to scattered plots.

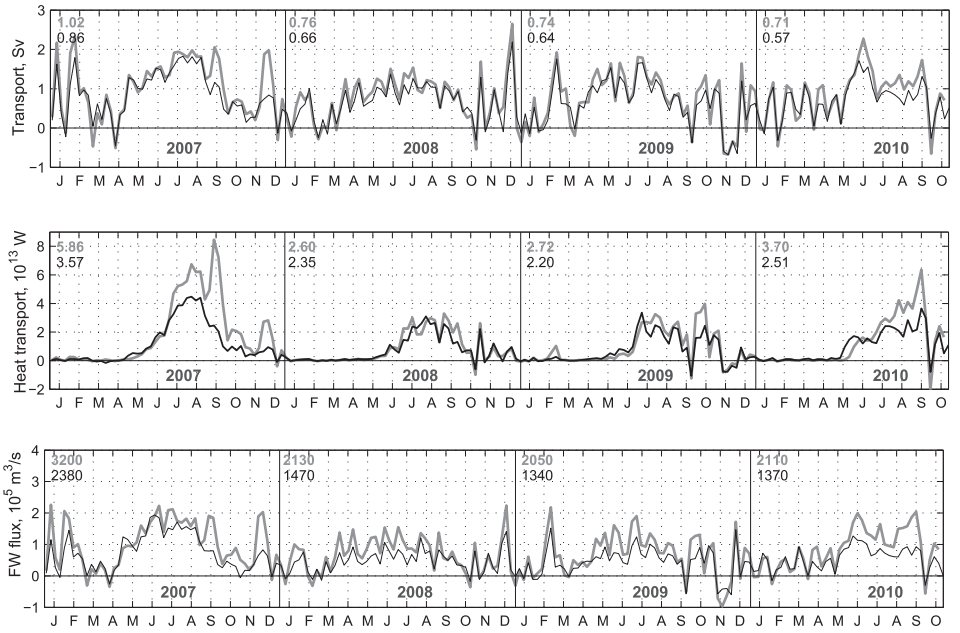

Figure 7. Evolution of the weekly averaged mass, heat and freshwater fluxes through the Bering (thick gray line) and Anadyr Straits (thin black line). Annual mean values of the fluxes are shown in the top left corners of the respective boxes. The units are respectively 10^6 m^3/s, 10^{20} J, and 10^3 km^3. The mean 2010 transport was calculated for a period of 10 months.

much better linear fit ($R = 0.86$) compared to the one characterizing the BESTMAS solution ($R = 0.53$). The BESTMAS velocities are significantly biased against the data for all groups of the velocity observations described above. The 4dVar velocities still have a small bias and that probably explains a somewhat smaller mean BST (cf. Figure 4) over the assimilation period.

Overall, we believe that the obtained 3.8 year estimate of the EBS state is one of the most dynamically and observationally consistent solutions among the existing data-assimilative model runs. This conclusion is based on a somewhat smaller distance of the obtained model trajectory from observations (Figure 4), better dynamical continuity of the 4dVar output compared to the results of sequential analyses delivered by ACNFS and BESTMAS, and a reasonable quantitative agreement of the presented solution with the above mentioned EBS estimates of similar resolution.

3.2. Mass, Heat, and Freshwater Transports

The 4dVar-optimized weekly averaged fluxes are shown in Figure 7 for the Bering and Anadyr Straits. Because the mass is conserved, and the surface heat/freshwater fluxes in the Chirikov basin can be neglected, the difference between the curves gives an insight on the partitioning of the respective Bering Strait transports between the Anadyr and Spanberg inflows. Heat and freshwater transports were obtained relative to -1.9°C and 34.8 psu, respectively.

In general, the obtained annual mean fluxes appear to be more consistent with the observational estimates than those extracted from the BESTMAS solution (see Table 1). One should also bear in mind that observational fluxes in Table 1 were derived from a single point observation.

Qualitatively, both models capture the 2008–2009 minimum of the transports documented by *Woodgate et al*. [2012]. However, there are large quantitative differences, which, in our opinion, favor the 4dVar solution. In particular, the BESTMAS transports appear to be underestimated, as they are 1.3–2 times smaller than the observed ones, and are very close to the values (0.65 Sv, $2.82 \cdot 10^{20}$ J/yr, 1480 km^3/yr), obtained in the climatological simulation conducted by *Clement et al*. [2005] for the previous two decades (1979–2001), when the net fluxes where not as large as, for example, in 2007.

It is also noteworthy that observational transport estimates in Table 1 [*Woodgate et al*., 2012] were obtained under rather crude assumptions on the spatial variation of the flow within the Bering Strait. In general, the annual mean observational estimates of *Woodgate et al*. [2012] appear to be somewhat 10–20% larger than

Table 1. Annual Mean Transports of Volume (M, Sv), Heat (H, 10^{20}J) and Freshwater (F, km^3) Through the Bering Strait in the 4dVar and BESTMAS Solutions[a]

	BESTMAS			4dVar			Obs*[b]		
	M	H	F	M	H	F	M	H	F
2007	0.76	4.49	1424	1.10	5.33	3380	1.05	5.30	2950
	0.08	0.09	0.07	0.15	0.26	0.26	±.08	±.3	±250
2008	0.57	1.74	836	0.72	3.08	2160	0.89	3.50	2250
	0.07	0.05	0.10	0.14	0.13	0.29	±.10	±.3	±250
2009	0.70	2.69	1303	0.83	3.00	2240	0.93	3.70	2700
	0.08	0.25	0.17	0.18	0.34	0.37	±.12	±.3	±250
2010	0.87	4.44	1518	0.70	4.14	2170	1.01	4.50	3300
	0.08	0.23	0.11	0.19	0.43	0.40	±.1	±.3	±250
mean	0.77	3.55	1357	0.84	3.88	2510	0.97	4.25	2800
	0.08	0.16	0.11	0.16	0.29	0.31	0.20*	0.36*	0.21*

[a]Lower numbers in columns 1–6 show relative contributions of the Spanberg Strait to the transports. Lower numbers in columns 7–9 of the last row show flux partitioning of the 23 year (1979–2001) simulation of *Clement et al.* [2005]

[b]Three columns on the right show observational estimates of *Woodgate et al.* [2012] with error bars. Estimates for 2010 should be multiplied by 0.8 to account for bias of the annual mean compared to the 10 month mean caused by higher summer transports.

those obtained by dynamically constrained interpolation of the same data (cf. columns 3–6 and 7–9 in Table 1). Similar tendency was observed by *Panteleev et al.* [2010] who compared 1990–1991 4dVar BST estimates with those obtained from a single mooring using heuristic methods of spatial extrapolation.

The notion that the data-derived transports in the last three columns of Table 1 are 10–20% overestimated is also supported by our analysis of the data (section 3.1) from the entire array of the Bering Strait moorings during the 34 month period between October 2007 and July 2010, when observations in the Russian channel were available. During this period, the refined observation-based estimate of the volume transport is 0.76 Sv (cf. Figure 4), a value 18% smaller than 0.94 Sv derived from averaging the observational 2008–2010 transports in the 7th column of Table 1. The fact that a single-point observation tends to overestimate BST is also supported by a tendency for a somewhat smaller Bering Strait transport in higher resolution models documented recently by *Clement-Kinney et al.* [2014].

The 4dVar partitioning of the BST between the Anadyr and Spanberg sources appears to be more close to the one obtained by *Clement et al.* [2005] than to BESTMAS (last line in Table 1). We attribute smaller BESTMAS transport contribution from the Spanberg Strait to the difference in the mean SSH pattern (cf. Figure 5). Due to predominantly barotropic nature of the circulation, the low BESTMAS volume transport results in certain underestimation of the Spanberg heat/freshwater fluxes enriched by warm and fresh riverine waters from Alaska.

An interesting feature in Figure 7 are a number of events when the Bering Strait fluxes were much larger than the advective heat/freshwater transports entering Chirikov Basin through the Anadyr Strait (e.g., September, November, December 2007, August–September 2010). Near-surface circulation and wind stress patterns (Figures 8a and 8c) indicate that these anomalies were caused by strong southeasterly winds over the EBS shelf, which raise sea level along the Alaskan coast and enhance transport of the warm and fresh waters through the Spanberg Strait.

Wind stress patterns in Figures 8a and 8c indicate that intensification of the northward current along the Alaskan coast was forced by atmospheric lows over the central Bering Sea. Such cyclones are quite common phenomena in late fall/winter and are known to cause intensification of the Kamchatka Current [*Hughes et al.*, 1974]. However, since the EBS water temperature is close to freezing in winter, these winds have little effect on the heat transport, but may cause a noticeable increase in the freshwater transport (Figure 7, bottom). In summer, strong southeasterly winds associated with cyclones over the BS basin are less common, although a certain increase in summer storm activity has been documented [*Mesquita et al.*, 2010] over the last decade. These storms may contribute significantly to the observed decrease of the ice cover in the Chukchi Sea. Compared to summer, winter storms have a larger impact on the deep mixing in the central BS and freshwater flux through the Bering Strait.

Another interesting phenomena in Figure 7 are the anomalous (southward) transport events through the Bering Strait. Most of them occur in fall-winter and have a typical duration of 1–2 weeks. An exception is a

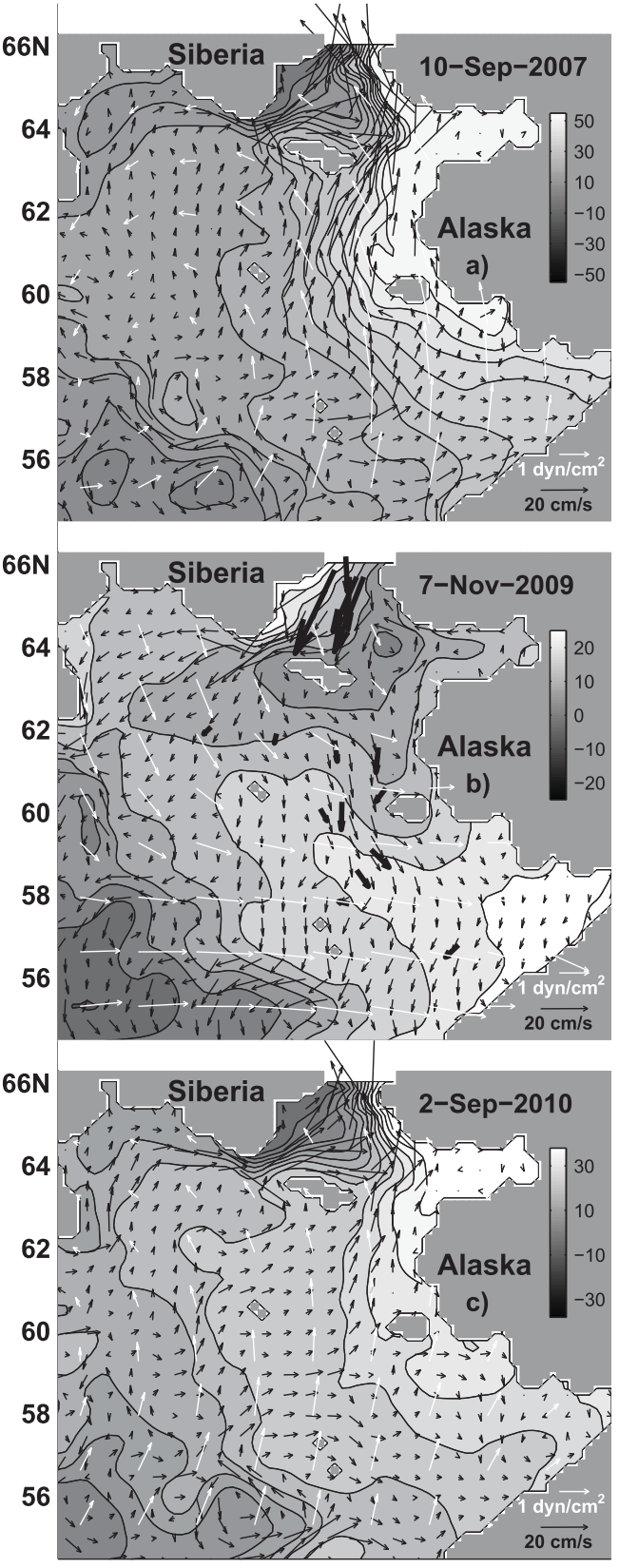

Figure 8. Velocity at 25 m depth (black arrows), wind stress (white arrows), and SSH (shading, cm), on 0.00 UTC on 10 September 2007, 7 November 2009, and 2 September 2010. Thick arrows in the middle plot show velocities observed at the moorings.

28 day long southward transport observed in November 2009. Comparison with the wind forcing has shown that all the negative anomalies in September–November of 2008–2010 are associated with southward winds. This phenomenon has been documented by *Coachman* [1993] and appears to be a typical feature for the freezing and (to a lesser extent) melting seasons. It is also remarkable that in 2007–2010 reversing of the Bering Strait throughflow mostly occurred in sync with the Anadyr current, when the contribution of the Spanberg Strait volume transport becomes negligible. Analysis of the optimized circulation shows that forcing by northeasterly winds completely blocks the Spanberg Strait throughflow, causing dramatic structural changes in the SSH and circulation patterns. Northwesterly wind surge tends to change the sign of the large-scale SSH gradient in the southern EBS (cf. Figures 8a–8c) and completely reverse the flow field in the Bering Strait along the Alaskan and Siberian coastlines. Prolonged flow reversals, such as the one observed in November 2009, may have a significant impact on the EBS ecosystem by affecting the residence times and displacing the cold pool [e.g., *Cianelli and Bailey*, 2005] boundary which is advected by the general southward flow clearly visible in Figure 8b on a larger scale.

3.3. Lagrangian Analysis

Another impact factor is related to bringing the Arctic waters deep into the BS basin. To estimate the extent of such penetration, we conducted Lagrangian analysis of circulation in the northern EBS during the 2009 reversal event. Lagrangian particles were continuously released during the first 2 days of the event on the transect across the Bering Strait. Their trajectories are shown in Figure 9. It is remarkable that all the particles eventually tend to follow a general pathway in the direction of the Anadyr Strait. Particles released in the eastern part of

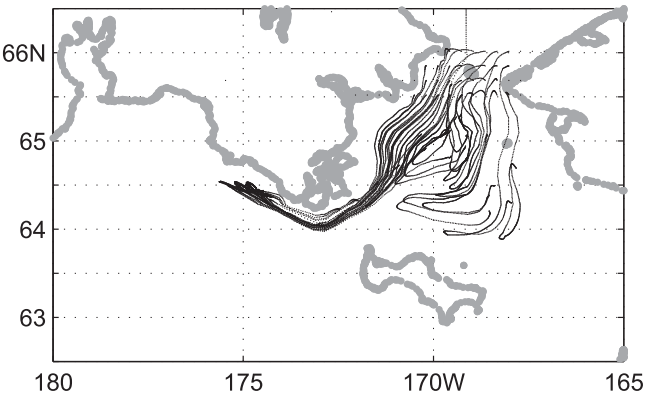

Figure 9. Trajectores of 25 particles launched at the section across the Bering Strait during the November 2009 flow reversal. Integration is performed from 3 November to 28 November 2009.

the transect have smaller southward velocities and end up in the middle of the Chirikov Basin by the time when north-easterlies calm down. Particles released in the western part of the Strait move much faster and are able to reach the Bay of Anadyr in 15–20 days and may eventually be engaged in the cyclonic circulation in the Bay.

Almost a 4 year time span of the presented reanalysis allows us to conduct a Lagrangian study on the time scales consistent with the largest residence times. This provides an opportunity to estimate basin-wide Lagrangian characteristics of the EBS circulation. It is well established that the major inflow into the Bering Sea occurs as the Alaskan current progresses along the chain of Aleutian Islands forming the North Aleutian Slope Current (NASC) [*Stabeno et al.*, 1999]. The latter is fed by the flows through numerous straits between the Aleutian islands. Upon reaching the continental slope, NASC turns northwest forming the BS Slope Current (BSC) which carries all the water which later discharges into the Arctic Ocean through the Bering Strait. Therefore, particle release at the BSC source around 54.5°N 165–170°W (Figure 10) provides an opportunity to trace the history of all the water entering the Arctic Ocean. Lagrangian analysis described below was made using the velocities from the coarse resolution model.

3.3.1. Pathways and Residence Times

In the numerical experiments we focused on two subregions: the Unimak Strait (the very first passage from the open Pacific into the EBS) and the BSC source region proper located north of Unalaska Island. Lagrangian particles were released in each region once a week during 3.5 years. Their trajectories were computed using the fourth order Runge-Kutta scheme.

Figure 10a shows typical trajectories of the particles released north of Unalaska Island. These particles are advected by the BSC and initially follow the 300 m isobath. Then they are involved into eddy-induced exchange across the EBS shelf [*Mizobata et al.*, 2006]. More than a half (4065) of the released particles (7600) leave the model domain through the Bering Strait with the remaining 3535 particles leaving go out through the western open boundary. Trajectories of the fastest particles that leave the region through the Bering Strait are shown by the black lines (Figure10a).

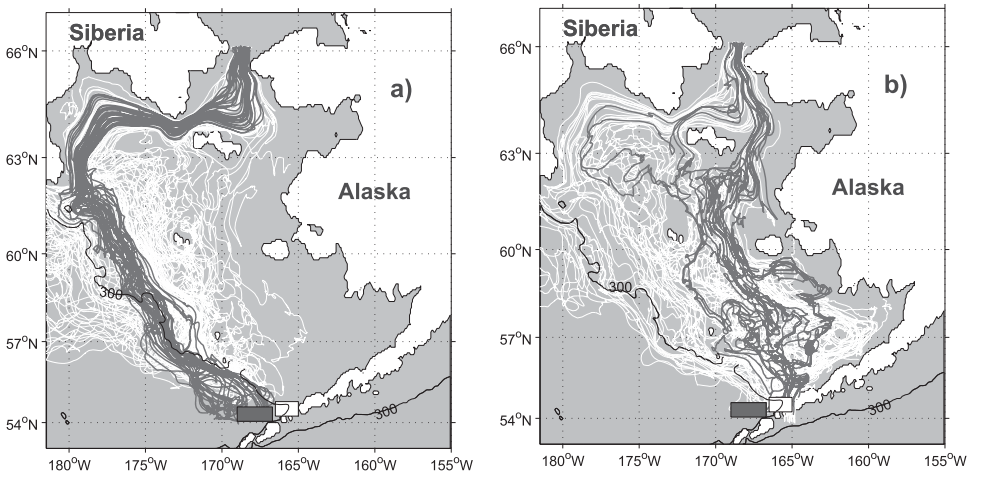

Figure 10. Trajectories of the particles released in in the Unimak Pass (light gray rectangle) and north of the Unalaska Island (dark gray). Solid lines designate the (a) fastest and (b) slowest trajectories of the particles reaching the Bering Strait.

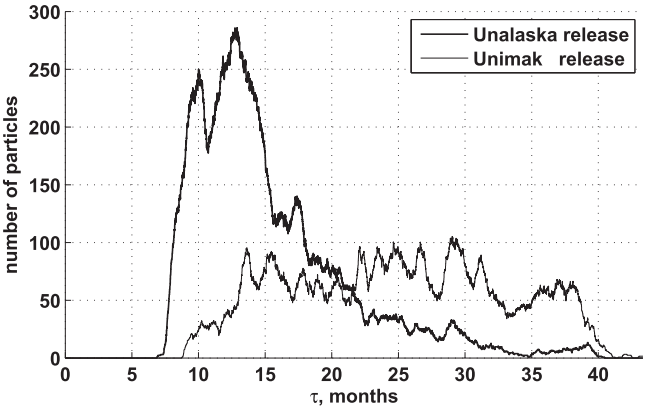

Figure 11. EBS residence time distribution of the particles released in the Unimak Pass (thin line) and north of Unalaska Island.

Particle trajectories from the Unimak Strait are shown in Figure 10b. Most of these particles stay in the EBS and never cross the 300m isobath. We found that only 13% of the released particles left the region through the western boundary while the remaining particles were transported into the Arctic Ocean through the multiple pathways on the EBS. Taking into account that the Unimak region is the major supplier of southern Bering Sea waters into the EBS, we can assume that ventilation of the southern EBS is driven by the slow and chaotic advection toward the Bering Strait with a minor contribution from the eddy-induced mixing across the continental slope. Trajectories of the slowest particles from this release are shown in Figure 10b by black lines. Note, that a considerable part of these trajectories cross the center of the cold pool region discussed below.

Such a contrasting behavior of the Lagrangian particles launched in two adjacent regions agrees well with statistics of surface drifters drouged at 40m and the surface circulation maps derived from their trajectories [*Stabeno and Reed*, 1994; *Schumacher and Stabeno*, 1998; *Stabeno and Van Meurs*, 1999; *Panteleev et al*., 2006]. The above mentioned splitting was also obtained in the Lagrangian analysis of the output of the regional ocean model [*Stabeno et al*., 2005]

It is also noteworthy that the largest residence times τ (up to 40 months) were observed exclusively for the particles released in the Unimak Pass while the smallest residence times (8–10 months) were documented for the particles released north of Unalaska Island, where NASC meets the EBS continental slope.

Residence time distributions (Figure 11) of the particles reaching the Bering Strait from both regions are quite different in shape. The Unalaska release region is characterized by the double peak structure. A more detailed analysis shows that the fastest particles, corresponding to the first peak at $\tau = 10$ months were mostly released in the fall season (October–November), when the BSC spins up by the Aleutian Low centered over the Bering Sea [*Wang et al*., 2004] and by intensifying storm activity [*Panteleev et al*., 2012; *Ladd*, 2014]. The majority of Unalaska released particles reach the Arctic Ocean in 11–15 months as they travel with BSC of normal strength. The near-exponential tail of the distribution ($\tau \sim 16 - 35$ months) is formed by the particles carried by mesoscale eddies across the continental slope into the EBS shelf [*Mizobata et al*., 2006].

In contrast to the Unalaska particles, particles released at Unimak Pass are characterized by much more homogeneous distribution over the residence times (thin line in Figure 11). This could be explained by the low probability of their capture by the BSC core. As a consequence, most of these particles start their journey in the EBS shelf environment which is characterized by much weaker and less organized currents. Trajectories of the Unimak Pass particles with the largest residence times ($\tau \sim 35$–40 months) shown in Figure 11 first wander around the southern EBS shelf west of Pribilof Islands, and then slowly proceed north following the Spanberg Strait pathway to the Arctic Ocean. Only a small fraction of these particles join the Anadyr current far downstream, and they are never engaged in the eddy-induced exchange with the BSC. The same property characterizes the fastest particles populating the left peak ($\tau < 11$ months) of the Unalaska distribution in Figure 11. These particles strictly follow the main stream of the BSC and Anadyr currents.

Most of the "intermediate" particles with residence times between 1 year and 3 years are involved in the eddy-induced exchange across the EBS shelf: their paths fill the gap that stretches northwestward between the dark trajectories in Figures 10a and 10b.

3.3.2. Source Regions

Geographic origins of the Pacific waters entering the Arctic Ocean could be estimated through the release of particles in the Bering Strait and tracking their motion in the reversed velocity field. Experiments of this

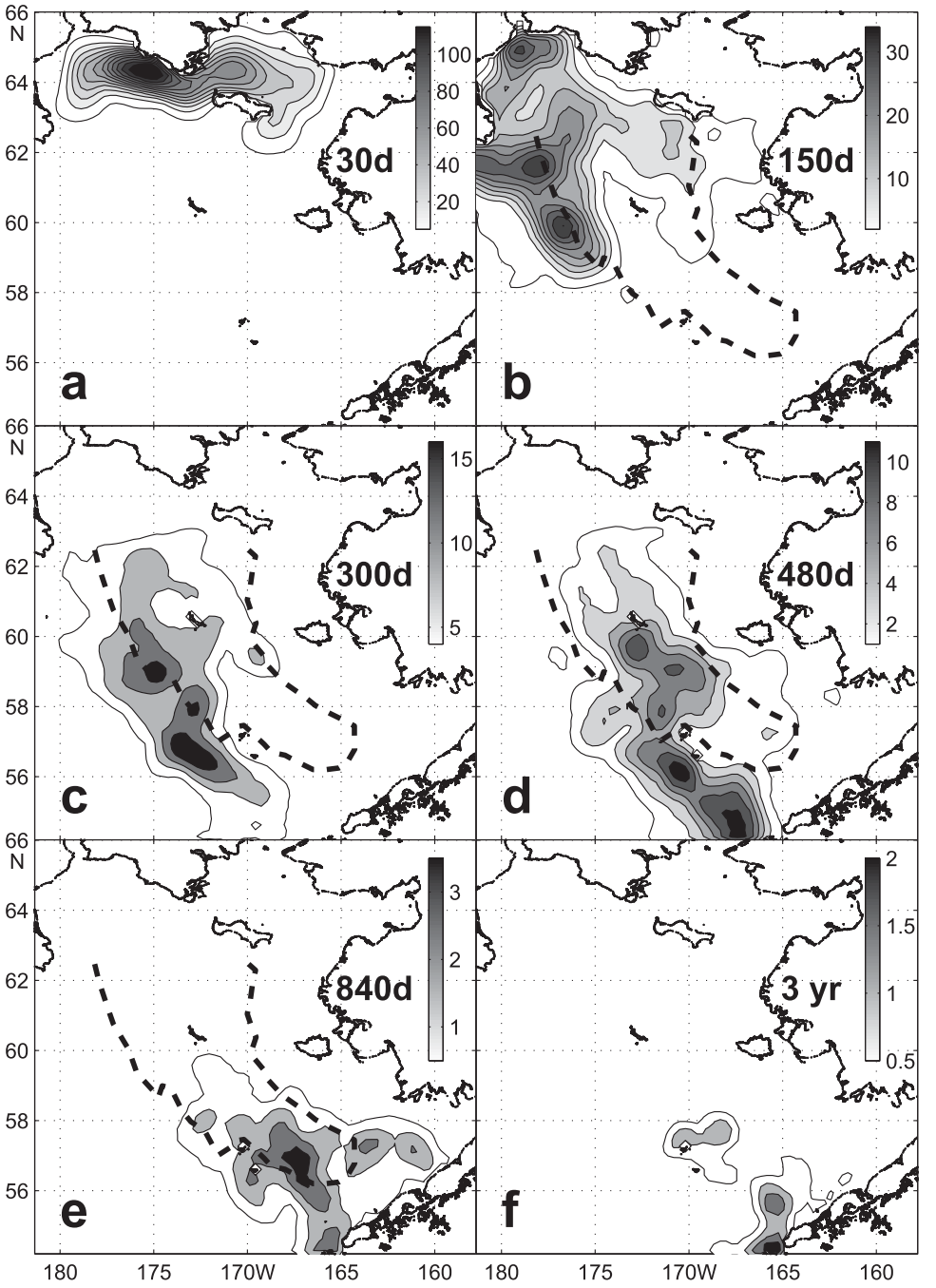

Figure 12. Source regions of Pacific water entering the Bering Strait after traveling for specific periods of time τ_p in the Bering Sea. The values of τ_p are shown on the right. Shading shows the number of particles per 50 × 50 grid cells. The 2007–2010 average cold pool location reconstructed by the 4Dvar reanalysis is shown by the dashed contour.

kind were done as follows: 20 particles were released daily at 25 m along the Bering Strait transect in the period between 3 October 2010 and 1 March 2007. Positions of the particles were computed, and their numbers were averaged over 50 km ×50 km grid cells for 10 day travel time τ_p windows.

Results of these computations are shown in Figure 12. At $\tau_p = 30$ days, there is a prominent source region in the Gulf of Anadyr, approximately 600 km upstream from the Bering Strait. This maximum particle concentration is a signature of the Anadyr current. A secondary maximum 250 km southwest of the Bering Strait can be partly attributed to the existence of the shadow zone on the leeward coast of the St. Lawrence Island.

At $\tau_p = 150$ days, the source region undergoes a significant expansion with the major maxima of particle concentration located approximately 150–300 km southeast of Cape Navarin. A significant source region can be also identified near the Anadyr river mouth. It is also noteworthy that Figure 12b has virtually no Arctic-bound particles in the cold pool region south of 62°N and east of 174°W. It is interesting to note, that advection of the particles into the cold pool takes place mostly through its western boundary, indicating the importance of eddy-induced mixing across the continental slope in the erosion of the cold pool. Advection through the north-eastern boundary of the cold pool is probably less intensive as it is characterized by the abundance of the paths attributed to the slowest particles released near the Unimak Strait (Figure10b).

Moving further backward in time, the maximum concentration of water parcels reduces dramatically (cf. black and white scale in Figures 12a and 12f). This phenomenon is caused by mesoscale eddy activity along the continental shelf break and losses of the Arctic-bound particles through the southern boundary. As the Arctic water source region progresses upstream BSC (Figures 12b and 12e), particle concentration increases in the cold pool, peaking around 480 days (Figure 12d).

At $\tau_p = 700$ days the number of Arctic-bound particles in the cold pool drops 30 times back to the values observed at $\tau_p = 150$ days. Also note that at $\tau_p = 480$ days, the particle concentration peaks north of Unalaska Island (167° – 171°W, cf. Figure 10), which is the source region of the BSC.

At $\tau_p = 840$ days (Figure 12e) the source region displaces eastward to the Unimak Pass occupying areas north and northeast of Aleutian Peninsula. At $\tau_p = 3$ years particle statistics becomes insufficient for confident identification of the source regions. The only possible exception is the region of Unimak Pass (Figure 12f).

The presented 4dVar reanalysis provides an opportunity for detailed studies of the Lagrangian transport in three dimensions. Of particular interest are the exchange processes between the EBS shelf and the Aleutian Basin of the Bering Sea. Preliminary computations indicate that the cross-shelf fluxes are especially prominent around 175°W and 178°E and have a pronounced seasonal variation. Additional computations and careful analysis of the error sources are, however, necessary to obtain confident quantitative estimates of the flux variability along the EBS shelf break.

4. Summary and Discussion

In the presented study we carried out a comprehensive 4dVar reanalysis of the Bering Sea state during the period between 1 January 2007 and 3 October 2010. Within this effort, nearly all available remotely sensed and in situ data were employed to constrain a numerical model configured at higher (7 km) resolution in the Bering Strait region. A novel two-way 4dVar nesting technique was applied to maintain consistent communication between the fine and coarse resolution grids in the process of model-data synthesis. This approach assured free exchange of information between the coarse grid in the south with abundant SSH and in situ data and the high-resolution grid with the mooring array in the Bering Strait, which provides a strong feedback to the southern grid through dynamical relationships.

Optimized evolution of the EBS circulation was validated against sequential data-assimilative products of similar spatial resolution (BESTMAS at 7 km and ACNFS at 10 km). Comparison have shown that 4dVar reanalysis is more consistent with the observed transports in the Bering Strait (Figure 4) and in the EBS interior (Figure 6) both in terms of their magnitude and time variability. Another advantage of the presented reanalysis is its better dynamical consistency, as it is not driven by the artificial forcing which attracts sequential data-assimilative solutions to the data.

We conducted preliminary analysis of the solution focusing on the variations in the EBS circulation caused by strong wind forcing events and on the Lagrangian tracking of the Pacific water in the EBS. The major results can be summarized as follows:

1. Two types of wind forcing events are responsible for significant reorganization of the EBS circulation. The first type is related to strong atmospheric cyclones most frequently observed in the fall and winter seasons. When their eastward movement slows down, these cyclones drive anomalous amounts of warm and fresh water through the Spanberg Strait that may cause freezing delays in the Chukchi Sea and/or excessive ice melt. In the analyzed time period, such events were most prominent in September–December 2007, October 2008, and July–September 2010 (Figure 7).

2. The second type of wind forcing events is associated with strong northwesterly winds. In 2007–2010, these events were less frequent but caused more significant changes in circulation. Of special interest was the anomalously long (25 days) event observed in November 2009. According to reanalysis, this event caused the complete reversal of the Bering Strait troughflow (Figure 8b), forcing Siberian Coastal Current waters to travel to the Gulf of Anadyr (Figure 9), where they could potentially be engaged in the southward reversal coastal flow [*Stabeno et al*., 1999] and reach Cape Navarin. Although events of such longevity may not be considered as typical, they may have a large impact on the ecosystem dynamics in the western EBS.
3. Lagrangian analysis of the Arctic-bound Pacific water particles have shown that the spectrum of particle routes lies between two extremes: The fastest parcels are dragged by BSC escaping the cross-shelf exchange by the eddies and then join the Anadyr Current near Cape Navarin. These particles reach the Bering Strait in 8–10 months and can typically be observed during the periods starting in September–October, when particle motion is propelled by the BSC spin-up forced by the fall-winter storms. Particles of this kind form a distinctive peak in the travel time distribution (Figure 11). The slowest particles enter EBS exclusively through the Unimak Pass and start their journey in the EBS shelf environment characterized by much less organized and weaker currents than those observed in the BSC. Their travel times may reach 3–3.5 years and their properties may significantly change during such a long period.

   The majority (80%) of Arctic-bound Pacific waters experience travel histories which lie in between these two extremes. The key playing factor for these waters is the eddy-induced exchange at the continental slope which ejects BSC parcels onto the shelf and conversely, engages the shelf waters in the BSC flow. A targeted Lagrangian analysis of this process indicates two "exchange gateways" located around 175°W and 178°E diagnosed earlier by *Okkonen* [2001], but confident quantitative estimates require more close scrutiny.

4. Application of the reverse Lagrangian technique to the reanalysis velocity fields allowed identification of the source regions for the Pacific waters with fixed residence times. Of particular interest is the result that typical residence times in the cold pool range between 9 and 20 months, that is 2–3 times larger than the travel times in the adjacent waters (Figures 12b–12d). Such a slow advection through the cold pool region explains its stability in summer and its persistence in maintaining the related features of the Bering Sea ecosystem.

   Complexity of the cross-shelf exchange processes and wind-current relationships in the region requires further in-depth studies of the EBS circulation. We believe that results of the presented reanalysis provide a capacity to gain quantitative understanding of the relevant physical processes. This is extremely important for ecological studies of one of the most productive regions in the World Ocean.

Appendix A: Convergence of the Nested 4dVar Algorithm

Adopting the notation $\tilde{\mathbf{H}}$ for the Hessian matrix and $\mathbf{x}^o$ for the (unique) optimal soltions of the uncoupled problems, the cost functions J^0 in both domains can be represented in the form

$$J^0=\frac{1}{2}(\mathbf{x}-\mathbf{x}^o)^{\mathsf{T}}\tilde{\mathbf{H}}(\mathbf{x}-\mathbf{x}^o) \tag{A1}$$

Suboptimal solutions on the nth iteration are obtaned by setting the gradients of (2–3) to zero:

$$\mathbf{x}_\Omega^n=(\tilde{\mathbf{H}}_\Omega+\gamma B_\Omega^{\mathsf{T}}B_\Omega)^{-1}(\tilde{\mathbf{H}}_\Omega\mathbf{x}_\Omega^o+\gamma B_\Omega^{\mathsf{T}}B_\omega\mathbf{x}_\omega^{n-1}) \tag{A2}$$

$$\mathbf{x}_\omega^n=(\tilde{\mathbf{H}}_\omega+\quad\mathbf{B}^{-1}\ )^{-1}(\tilde{\mathbf{H}}_\omega\mathbf{x}_\omega^o+\ \mathbf{B}^{-1}\mathbf{P}\mathbf{x}_\Omega^{n-1}) \tag{A3}$$

where B_Ω and B_ω are the row vectors representing BST operators on the respective grids.

Introducing notations $\mathbf{y}:=\{\mathbf{x}_\Omega,\mathbf{x}_\omega\}^{\mathsf{T}}$, $\mathbf{D}:=\mathrm{diag}\{\mathbf{D}_\Omega,\mathbf{D}_\omega\}$ with $\mathbf{D}_\Omega=(\mathbf{I}_\Omega+\gamma\tilde{\mathbf{H}}_\Omega B_\Omega^{\mathsf{T}}B_\Omega)^{-1}$, $\mathbf{D}_\omega=(\mathbf{I}_\omega+\tilde{\mathbf{H}}_\omega\mathbf{B}^{-1})^{-1}$ and $\mathbf{I}_\omega,\mathbf{I}_\Omega$ standing for the identity matrices in the respective domains, equations (A2) and (A3) can be rewritten in the form

$$\mathbf{y}^n=\mathbf{D}(\mathbf{Q}\mathbf{y}^{n-1}+\mathbf{y}^o) \tag{A4}$$

where

$$\mathbf{Q}=\begin{bmatrix} \mathbf{0} & \gamma\tilde{\mathbf{H}}_{\Omega}^{-1}B_{\Omega}^{\mathsf{T}}B_{\omega} \\ \tilde{\mathbf{H}}_{\omega}^{-1}\mathbf{B}^{-1}\mathbf{P} & \mathbf{0} \end{bmatrix} \tag{A5}$$

Since eigenvalues of **DQ** are continuous functions of γ, the value of γ can always be chosen to satisfy the convergence criterion (spectral radius of **DQ** ≤ 1) in which case the iterative procedure (A4) convereges to the unique solution $\mathbf{y}^{\infty}=(\mathbf{I}-\mathbf{DQ})^{-1}\mathbf{D}\mathbf{y}^{o}=(\mathbf{D}^{-1}-\mathbf{Q})^{-1}\mathbf{y}^{o}$.

Acknowledgments
This study was supported by International Arctic Research Center, NSF grants 1107925, 1203740, and ARC-1107327. Max Yaremchuk was supported by the ONR core projects" Adjoint-free 4dvar for navy ocean models" and" Coupled data assimilation." We further thank the support of the Russia government (megagrant 2013-220-04-157). The authors are indebted to R. Woodgate of APL UW for providing current meter data in the Bering Strait. The results of the reanalysis can be downloaded from http://people.iarc.uaf.edu/gleb/best_reanalysis/final_report/final_report.htm).

References

Allard, R., P. Posey, R. Preller, D. Hebert, E. J. Metzger, A. Walcraft, S. Piacsek, O. M. Smetstad, and M. Phelps (2012) The Arctic Cap nowcast forecast system, *Geophys. Res. Abstr.*, *14*, EGU2012-2160.

Brasseur, P. (1991), A variational method for the reconstruction of general circulation fields in the Northern Bering Sea, *J. Geophys. Res.*, *96*, 4891–4907.

Brasseur, P., and K. Hausk (1991), Application of the three-dimensional variational inverse model to the analysis of ecohydrodynamic data in the Bering and Chukchi seas, *J. Mar. Syst.*, *1*, 383–401.

Cianelli, L., and K. M. Bailey (2005), Landscape dynamics and resulting species interactions: The cod-capelin system in the southeastern Bering Sea, *Mar. Ecol. Prog. Ser.*, *291*, 227–236.

Clement, J. L., W. Maslowski, L. W. Cooper, J. M. Grebmeier, and W. Walczowski (2005), Ocean circulation and exchanges through the Northern Bering Sea––1979-2001 model results, *Deep Sea Res., Part II*, *52*, 3509–3540.

Clement-Kinney, J. L., W. Maslowski, Y. Aksenov, B. Cuevas, J. Jakacki, A. Nguyen, R. Osinski, M. Steele, R. A. Woodgate, and J. Zhang (2014), On the flow through the Bring Strait: A synthesis of model results with observations, in *The Pacific Arctic Region*, edited by J. M. Grebmeier, W. Maslowski, pp. 167–198, Springer.

Coachman, L. K. (1993), On the flow field in the Chirikov Basin, *Cont. Shelf Res.,. 13*(5/6), 481–508.

Danielson, S. L., E. Curchitser, K. S. Hedstrom, T. Weingartner, and P. Stabeno (2011), On ocean and sea ice modes of variability in the Bering Sea, *J. Geophys. Res.*, *116*, C12034, doi:10.1029/2011JC007389.

Danielson, S. L., K. S. Hedstrom, K. Aagaard, T. Weingartner, and E. Curchitser (2012a), Wind-induced reorganization of the Bering shelf circulation, *Geophys. Res. Lett.*, *39*, L08601, doi:10.1029/2012GL051231.

Danielson, S. L., T. Weingartner, K. Aagaard, J. Zhang, and R. Woodgate (2012b), Circulation on the central Bering Sea shelf, July 2008 to July 2010, *J. Geophys. Res.*, *117*, C10003, doi:10.1029/2012JC008303.

Danielson, S. L., T. J. Weingartner, K. S. Hedstrom, K. Aagaard, R. Woodgate, E. Curchitser, and P. J. Stabeno (2014), Coupled wind-forced controls of the Bering-Chukchi shelf circulation and the Bering Strait throughflow: Ekman transport, continental shelf waves, and variations of the Pacific-Arctic sea surface height gradient, *Prog. Oceanogr.*, *125*, 40–61.

Donlon, C. J., M. Martin, J. D. Stark, J. Roberts-Jones, E. Fiedler, and W. Wimmer (2011), The operational sea surface temperature and sea ice analysis (OSTIA), *Remote Sens. Environ.*, *116*(1), 140–158.

Durski, S. M., A. Kurapov, J. Zhang, and G. Panteleev (2015), Circulation in the Eastern Bering Sea: Inferences froma 2-kilometer-resolution model, *Deep Sea Res., Part II*, doi:10.1016/j.dsr2.2015.02.002, in press.

Ezer, T., and L.-Y. Oey (2010), The role of the Alaskan Stream in modulating the Bering Sea climate, *J. Geophys. Res.*, *115*, C04025, doi:10.1029/2009JC005830.

Grebmeier, J. M., and W. Maslowski (Eds.) (2014), *The Pacific Arctic Region*, 446 pp., Springer, N. Y., doi:10.1007/978-94-017-8863-25.

Guidard, V., and C. Fischer (2008), Introducing the coupling information in a limited-area variational assimilation, Quarterly Journal of the Royal Meteorological Society, *134*(632), 723–735, doi:10.1002/qj.215.

Hu, H., and J. Wang (2010), Modeling effects of tidal and wave mixing on circulation and thermohaline structures in the Bering Sea: Process studies, *J. Geophys. Res.*, *115*, C01006, doi:10.1029/2008JC005175.

Hughes, F. W., L. K. Coachman, and K. Agaard (1974), Circulation, transport and water exchange in the western Bering Sea, in *Oceanography of the Bering Sea With Emphasis on Renewable Resources*, edited by D. W. Hood and E. J. Kelley, pp. 59–98, Inst. of Mar. Sci., Univ. of Alaska, Fairbanks.

Janekovic, I., B. S. Powell, D. Matthews, M. A. Mcmanus, and J. Sevadijan (2013), 4D-Var data assimilation in a nested, coastal model: A Hawaiian case study, *J. Geophys. Res. Oceans*, *118*, 5022–5035, doi:10.1002/jgrc.20389.

Ladd, C. (2014), Seasonal and interannual variability of the Bering Slope Current, *Deep Sea Res., Part II*, *109*, 5–13.

Ladd, C., and N. Bond (2002), Evaluation of the NCEP/NCAR reanalysis in the NE Pacific and at the Bering Sea, *J. Geophys. Res.*, *107*(C10), 3158, doi:10.1029/2001JC001157.

Lindsay, R. W., and J. Zhang (2006), Assimilation of ice concentration in an ice-ocean model, *J. Atmos. Oceanic Technol.*, *23*, 742–749.

Mesquita, M. S., D. E. Atkinson, and K. I. Hodges (2010), Characteristics and variability of the storm tracks in the North Pacific, Bering Sea and Alaska, *J. Clim.*, *23*, 294–311, doi:10.1175/2009/JCLI3019.1.

Mizobata, K., J. Wang and S.-I. Saitoh (2006), Eddy-induced cross-slope exchange maintaining summer high productivity of the Bering Sea shelf break, *J. Geophys. Res.*, *111*, C10017, doi:10.1029/2005JC003335.

Nihoul, J. C. J., P. Adam, P. Brasseur, E. Deleersnijder, S. Djenidi, and J. Haus (1993), Three dimensional general circulation model of the northern Bering Seas summer ecohydrodynamics, *Cont. Shelf Res.*, *13*, 509–542.

Okkonen, S. R. (2001), Altimeter observations of the Bering Slope Current eddy field, *J. Geophys. Res.*, *106*, 2465–2476.

Panteleev, G., P. Stabeno, V. A. Luchin, D. Nechaev, and M. Ikeda (2006), Summer transport estimates of the Kamchatka Current derived as a variational inverse of hydrophysical and surface drifter data, *Geophys. Res. Lett.*, *33*, L09609, doi:10.1029/2005GL024974.

Panteleev, G., D. A. Nechaev, A. Proshutinsky, R. Woodgate, and J. Zhang (2010), Reconstruction and analysis of the Chukchi Sea circulation in 1990–1991, *J. Geophys. Res.*, *115*, C08023, doi:10.1029/2009JC005453.

Panteleev, G., M. Yaremchuk, P. J. Stabeno, V. Luchin, D. A. Nechaev, and T. Kikuchi (2011a), Dynamic topography of the Bering Sea, *J. Geophys. Res.*, *116*, C05017, doi:10.1029/2010JC006354.

Panteleev, G., V. Luchin, P. Stabeno, D. Nechaev, and T. Kikuchi (2011b), Climatological oceanographic atlas of the Bering Sea. [Available at http://research.iarc.uaf.edu/coabs/.]

Panteleev, G., M. Yaremchuk, V. Luchin, D. A. Nechaev, and T. Kikuchi (2012), Variability of the Bering Sea circulation in the period 1992–2010, *J. Oceanogr.*, *68*, 485–496, doi:10.1007/s10872-012-0113-0.

Panteleev, G., V. Luchin, N. P. Nezlin, and T. Kikuchi (2013), Seasonal climatologies of oxygen and phosphates in the Bering Sea reconstructed by variational data assimilation approach, *Polar Sci.*, *7*, 214–232.

Panteleev, G. G., B. de Young, C. Reiss, and C. Taggart (2004), Passive tracer reconstruction as a least squares problem with a semi-Lagrangian constraint: An application to fish eggs and larvae, *J. Mar. Res.*, *62*, 787–878.

Panteleev, G., M. Yaremchuk, and D. Nechaev (2009), Optimization of mooring observations in Northern Bering Sea, *Dyn. Atmos. Oceans*, *48*(1–3), 143–154.

Posey, P., E. J. Metzger, A. Walcraft, R. Preller, O. M. Smetstad, and M. Phelps (2010), Validation of the 1/12° Arctic Cap nowcast forecast system (ACNFS), *Tech. Rep. NRL/MR/7320-10-9287*, 55 pp., Naval Res. Lab., MAX ETO TVOE PRO PUSKU, Stennis Space Center, Miss.

Rayner, N. A., D. E. Parker, E. B. Horton, C. K. Folland, L. V. Alexander, D. P. Rowell, E. C. Kent, and A. Kaplan (2003), Global analyses of sea surface temperature, sea ice, and night marine air temperature since the late nineteenth century, *J. Geophys. Res.*, *108*(D14), 4407, doi: 10.1029/2002JD002670.

Roach, A. T., K. Aagaard, C. H. Pease, S. S. Salo, T. Weingartner, V. Pavlov, and M. Kulakov (1995), Direct measurements of transport and water prop- erties through Bering Strait, *J. Geophys. Res.*, *100*, 18,443-18,457.

Schumacher, J. D., and P. J. Stabeno (1998), Continental shelf of the Bering Sea, in *The Sea: Vol. 11, The Global Coastal Ocean: Regional Studies and Synthesis*, pp. 789–822, John Wiley, N. Y.

Stabeno, P., E. V. Farley, N. B. Kachel, S. Moore, C. Mordy, J. M. Napp, J. E. Overland, A. Pinchuk, and M. F. Sigler (2012), A comparison of the physics of the northern and southern shelves of the eastern Bering Sea and some implications for the ecosystem, *Deep Sea Res., Part II*, *65–70*, 14–30.

Stabeno, P. J., and R. K. Reed (1994), Circulation in the Bering Sea basin observed by satellite-tracked drifters: 1986-1993, *J. Phys. Oceanogr.*, *24*, 848–854.

Stabeno, P. J., and P. Van Meurs (1999), Evidence of episodic on-shelf flow in the southeastern Bering Sea, *J. Gephys. Res.*, *104*, 29,715–29,720.

Stabeno, P. J., J. D. Schumacher, and K. Ohtani (1999), The physical oceanography of the Bering Sea, in *Dynamics of the Bering Sea*, 838 pp., Alaska Sea Grant Coll. Program, Fairbanks.

Stabeno, P. J., N. A. Bond, N. K. Kachel, S. A. Salo, and J. D. Schumacher (2001), On the temporal variability of the physical environment over the southeastern Bering Sea, *Fish. Oceanogr.*, *10*(1), 81–98.

Stabeno, P. J., G. L. Hunt Jr., J. M. Napp, and J. D. Schumacher (2005), Physical forcing of ecosystem dynamics on the Bering Sea Shelf, NOAA, Chapter 30 in The Sea, Vol. 14, edited by A. R. Robinson and K. Brink.

Stabeno, P. J., J. Napp, C. Mordy, and T. Whitledge (2010), Factors influencing physical structure and lower trophic levels of the Eastern Bering Sea shelf in 2005: Sea ice, tides, and winds, *Prog. Oceanogr.*, *85*(3-4), 180–196.

Stark, J. D., C. J. Donlon, M. J. Martin, and M. E. McCulloch (2007), Ostia: An operational, high resolution, real time, global sea surface temperature analysis system, in OCEANS 2007-Europe, pp. 1–4, IEEE, Aberdeen, doi:10.1109/OCEANSE.2007.4302251.

Stroh, J. N., G. Panteleev, S. Kirillov, M. Makhotin, and N. Shakhova (2016), Sea-surface temperature and salinity product comparison against external in situ data in the Arctic Ocean, *J. Geophys. Res. Oceans*, *120*, 7223–7236, doi:10.1002/2015JC011005.

Wang, J., M. Jin, D. Musgrave, and M. Ikeda (2004), A numerical hydrological digital elevation model for freshwater discharge into the Gulf of Alaska, *J. Geophys. Res.*, *109*, C07009, doi:10.1029/2002JC001430.

Wang, J., H. Hu, K. Mizobata, and S.-I. Saitoh (2009), Seasonal variations of sea ice and ocean circulation in the Bering Sea: A model-data fusion study, *J. Geophys. Res.*, *114*, C02011, doi:10.1029/2008JC004727.

Wang, J., et al. (2013), A modeling study of seasonal variations of sea ice and plankton in the Bering and Chukchi Seas during 2007–2008, *J. Geophys. Res. Oceans*, *118*, 1520–1533, doi:10.1029/2012JC0088322.

Woodgate, R. A., K. Aagaard and T. Weingartner (2005), Monthly temperature, salinity, and transport variability of the Bering Strait through flow, *Geophys. Res. Lett.*, *32*, L04601, doi:10.1029/2004GL021880.

Woodgate, R. A., T. J. Weingartner, and R. Lindsay (2012), Observed increases in Bering Strait oceanic fluxes from the Pacific to the Arctic from 2001 to 2011 and their impacts on the Arctic Ocean water column, *Geophys. Res. Lett.*, *39*, doi:10.1029/2012GL054092.

Woodgate, R. A., K. M. Stafford, and F. G. Prahl (2015), A synthesis of year-round interdisciplinary mooring measurements in the Bering Strait (1990–2014) and the RUSALCA years (2004–2011), *Oceanography*, *28*(3), 46–67, doi:10.5670/oceanog.2015.57.

Yaremchuk, M., and A. Sentchev (2012), Multi-scale correlation functions associated with polynomials of the diffusion operator, *Q. J. R. Meteorol. Soc.*, *138*, 1948–1953.

Zador, S., et al. (2012), *PMEL/NOAA Report Ecosystem Considerations for 2012*. [Available at http://www.afsc.noaa.gov/refm/docs/2012/ecosystem.pdf.]

Zhang, J., and D. A. Rothrock (2001), A thickness and enthalpy distribution sea ice model, *J. Phys. Oceanogr.*, *31*, 2986–3001.

Zhang, J., and D. A. Rothrock (2005), The effect of sea ice rheology in numerical investigations of climate, *J. Geophys. Res.*, *110*, C08014, doi:10.1029/2004JC002599.

Zhang, J., R. Woodgate, and R. Moritz (2010), Sea ice response to atmospheric and oceanic forcing in the Bering Sea, *J. Phys. Oceanogr.*, *40*, 1729–1747.